Proceedings of the ASME 2020 15th International Manufacturing Science and Engineering Conference
MSEC2020
September 3, 2020, Virtual, Online

MSEC2020-8475

POWDER THERMAL CONDUCTIVITY MEASUREMENTS IN L-PBF USING POWDER-INCLUDED BUILD SPECIMENS: INTERNAL GEOMETRY EFFECT

Shanshan Zhang[a, 1], Brandon Lane[b], Kevin Chou[a]
[a] Department of Industrial Engineering
University of Louisville, Louisville, KY, 40292
[b] Engineering Laboratory, National Institute of Standards and Technology
Gaithersburg, MD, 20899

ABSTRACT

This study investigates the thermal conductivity of 17-4PH stainless steel powder that was encapsulated within specimens with different internal geometries in laser powder bed fusion (L-PBF) additive manufacturing (AM). The objective is to evaluate the effect of the internal geometry of the specimens on the measurement of the powder thermal conductivity and to compare the thermal properties amongst the 17-4PH and two additional powder materials used in L-PBF. Continued from the previous work [1], three new cone configurations in the hollow specimens were designed and fabricated in an L-PBF system. The thermal conductivity of the internal powder was indirectly measured using an experimental-numerical approach, combined with laser-flash testing, finite element (FE) heat transfer modeling and multivariate inverse method. The results reveal that the thermal conductivity of 17-4PH powder ranges from 0.67 W/(m·K) to 1.34 W/(m·K) at 100 °C to 500 °C, and varies with the internal geometry of the specimens. In addition, the measurement of the hollow specimen with a convex cone seems to be a more reliable evaluation. Further, the thermal conductivity ratio of the powder to the solid counterpart of 17-4PH approximately ranges from 3.9 % to 5.5 % at tested temperatures, which is similar to the results obtained from the nickel-based super alloy 625 (IN625) and Ti-6Al-4V (Ti64) powders measured in a previous study.

Keywords: Laser powder-bed fusion; laser flash; finite element modeling; inverse method; powder thermal conductivity; 17-4PH stainless steel

1. INTRODUCTION

Powder bed fusion (PBF) additive manufacturing (AM) is ever-increasingly investigated and widely adopted in recent years because of its capability to fabricate solid freeform shaped parts and high quality products for a wide range of applications. During the building process, metallic powder is spread onto the building plate and successive layers of powder are selectively fused by a high-energy heat source [2]. The thermal transfer between the melted part and the surrounding powder bed have a profound impact on the temperature gradient and the solidification rate, which in turn, gives rise to a substantial influence on the grain growth and microstructural morphology [3-6] and resultant mechanical properties of the final part [7, 8]. In addition, the powder bed acts as a support for overhanging structures in PBF, but also acts as a thermal insulator. This creates localized overheating, dependent on the relative amount of solid compared to powder material near the melt pool [9, 10]. Owing to the high cost of PBF equipment and materials, researchers seek assistance from the computational approaches to understand the thermal behavior in PBF processes, and consequentially to improve the fabrication processes and part quality. A key input for building these simulations is the thermal properties of the powder bed, which are essential to achieve reliable computational predictions.

Spread by the recoater and infiltrated by an inert gas environment in PBF, the powder bed can be regarded as a mixture of gas-infiltrated particles with a specific packing density. The individual properties of the metal powder, gas, and packing density can be combined to form an assumed continuum or singular material. For decades, many have recognized the dominant role of conduction in the heat transfer in heterogeneous gas-solid systems in different types of application processes, such as chemical reactors [11, 12], drying systems [13] and heat exchangers [14]. It has been reported that many factors can be critical, such as volume fraction, contacts between particles, infiltrated gas types and gas pressure [15-22]. For example, Yagi et al. [18] established a model of heat transfer in packed bed with

[1] Contact author: shanshan.zhang@louisville.edu

motionless gas. They raised theoretical equations to predict the effective thermal conductivities of a gas-powder packed bed system and concluded that the radiant heat transfer is more effective when the temperature is higher than 400 °C. Wakao and Vortmeyer [20] claimed that the effective thermal conductivity of packed beds with stagnant gas is primarily affected by the conductivity of the packed bed and radiation in the gas-solid system, as well as the contact conductivity between particles. A discrete element method in granular material heat transfer was developed by Vargas and McCarthy [22], which considered the effect of stress and contact heterogeneities on the pressure distribution in the stacked particles. On the other hand, Wei et al. [23] and Bala et al. [24] presented an experimental method to measure the thermal conductivities of metallic powders, and the latter pointed out that the gas infiltrating has an effect to the heat dissipation of the powder bed.

Recent studies by Cheng et al. [25] and Zhang et al. [1, 26] estimated the thermal conductivity of metallic powder using a hybrid laser flash experiment and numerical heat transfer simulation. In that work, the authors designed a hollow specimen to encapsulate powder during fabrication to maintain the in-situ powder bed conditions. Using an inverse heat transfer approach, the thermal properties of the encapsulated powder could be extracted from the laser flash measurement results. Herein, except for the thermal conductivity and powder porosity, the contact conductance between powder and the specimen shell was also critical to the heat transfer analyses and evaluated as an output. Additionally, a critical finding in those studies was that the powder thermal conductivity obtained by this method seems to be varied for different internal geometries of specimens. It was noted that a gap exists between the internal powder and the top shell of the specimen, which adversely affects heat flow through the specimen. Although this finding provides an insight of measurement uncertainty potentially related to the specimen geometry, quantitative understanding of the specimen internal geometry effect on the powder thermal property analysis is still lacking.

To continue the previous work, the objective is to design addition specimen geometries to investigate their effects on the measurement of powder thermal properties. In addition, the contact conductance between the powder and internal surfaces of specimen shell with different geometries are of interest. Furthermore, the experimental-numerical approach is extended to investigate the temperature-dependent thermal conductivity of 17-4PH stainless steel powder. A comparison of powder thermal conductivity and porosity with two additional powder materials: nickel-based super alloy 625 (IN625) and Ti-6Al-4V (Ti64), presents different results in a tested temperature range of 100 °C to 500 °C.

2. EXPERIMENTAL DETAILS

The test specimens were designed hollow discs that enclosed powder, thus maintaining the as-fabricated powder conditions. As indicated in [25], a cone feature can reduce the gap and improve the contact condition between the powder and internal upper shell, and therefore, increase the accuracy of simulation. However, the follow-up investigation in [1] showed inconsistent measured thermal conductivity of metallic powder, including IN625 and Ti64 materials, at specimens with three different internal geometries. To clarify the effect of the internal geometry of the specimens, the three shaped internal geometries were also tested in this study for estimating the powder properties of 17-4PH powder. In addition, 3 developed geometric features were designed as shown in Figure 1, including (1) top cone with a height of 1 mm (1Cone-1.0), (2) spherical cap with a height of 1 mm (Convex), and (3) concave, rotated cap with the height of 1 mm (Concave). These three novel specimens only vary the top internal geometry and keep the same bottom geometry to test the contact conditions between the powder and the top shell, specifically.

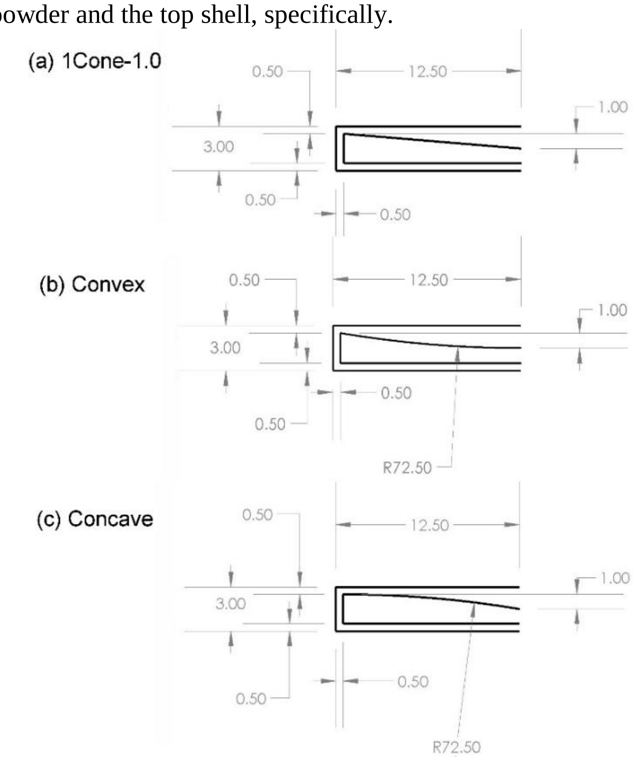

FIGURE 1: SYMMETRICAL CROSS-SECTION VIEW OF DIFFERENT SPECIMEN DESIGNS SHOWING INTERNAL GEOMETRY (UNIT: MM)

In this study, 17-4PH stainless steel supplied by LPW Technology[2] was used for specimen fabrication by an EOSINT M270 L-PBF system. The build orientation for the specimens

[2] Certain commercial equipment, instruments, or materials are identified in this paper in order to specify the experimental procedure adequately. Such identification is not intended to imply recommendation or endorsement by the National Institute of Standards and Technology, nor is it intended to imply that the materials or equipment identified are necessarily the best available for the purpose.

was along the diameter direction (along the horizontal axis in Figure 1) to reduce the necessity of support structure. The machine recommended process parameters for 17-4PH solids were used, resulting in a scan speed of 1000 mm/s, a laser power of 195 W, hatch spacing of 100 µm, and a layer thickness of 20 µm. There was no laser exposure within the internal hollow region to encapsulate loose powder. In addition, a N_2 inert gas environment was employed during fabrication.

A DLF-1200 laser flash system from TA Instruments was utilized to acquire thermograms from each sample, which indicate the time-dependent temperature rise measured via pyrometer on one side of the sample resulting from an applied laser pulse on the other. Thermal diffusivity values, representing the homogeneous properties of the entire sample, are extracted using Clark-Taylor method [27] in this study. Before testing, a graphite coating was uniformly sprayed on the sample surface to maximize the absorption of the laser pulse. The sample was then put into the chamber sitting in a sample holder. During testing, the ambient temperature in the chamber, which also sets the sample temperature, was a user-defined preset. When the environment and sample temperatures reach steady-state and equilibrium, a 3 ms laser pulse of 25 J was applied to the bottom of the specimen over a uniformly distributed, circular region of 22 mm diameter. An infrared pyrometer received the voltage signal from the top of the specimen from a round region with a diameter of about 9.6 mm for 60 s. The time-dependent voltage signal, called a thermogram, was then obtained and normalized for use in the inverse-heat transfer simulation. Three samples for each type of internal geometry and three laser pulses for each sample were conducted in the laser flash system for a repeatability investigation at each preset temperature. The tested temperatures ranged from 25 °C to 500 °C.

3. Test sample system and FE model

Test samples used in the FE model were dimensionally equal to the real test components, which were assumed homogeneous materials in the modeling. The mesh for the sample system consists of 10-node quadratic heat transfer tetrahedron bricks, with the mesh sizes of 0.5 mm for the specimen and 0.7 mm for the holder, respectively. The total heat flux applied to the bottom surface of the specimen was simplified as a uniform distribution. The heat transfer takes place through three mechanisms: (1) heat conduction in the specimen, (2) heat conduction between the specimen and the holder, and (3) heat loss due to convection and thermal radiation from the sample system to the surrounding environment. The ambient temperature in the modeling was set the same as the actual experimental environment. Further details on the FE model construction are provided in [1].

To calculate the thermal properties of the internal powder, there existed five unknowns in the FE model: (1) the specimen-holder contact conductance (k_p), (2) powder density (ρ), (3) powder thermal conductivity (k), (4) the contact conductance between the powder and the top solid shell (k_t), and (5) the contact conductance between the powder and the bottom solid shell (k_b). Two major steps were conducted to estimate the five unknowns. First, the solid sample system was simulated and measured to analyze the k_p, in order to simplify the model and reduce the computational workload. Then, the k_p in the solid sample system was assumed the same values in the powder-enclosed sample system at each corresponding temperature, and utilized as a known parameter in the latter model. Next, the remaining four unknowns related to the powder were estimated using an experimental-numerical inverse heat transfer method, originally derived in [28], and applied to the laser flash system as described in [25]. To optimize the estimated powder properties, the multivariate inverse method was adopted to evaluate a set of unknown properties in each iteration and reduce the difference between the simulation and experimental results.

4. RESULTS AND DISCUSSION

4.1 Laser flash experimental results

The specimens with different internal geometries were measured in the laser flash system at environment temperature range of 25 °C to 500 °C. Figure 2 shows the effective homogeneous sample thermal diffusivity on the three new designed specimen geometries, which are obtained from the laser flash instrument using the Clark-Taylor analytical model. The resulting diffusivity ascends with the rising temperature from 25 °C to 300 °C, and then a plateau occurs when the temperature continues increasing until 400 °C, and then a slight increase at 500 °C. The values range from 0.0018 cm^2/s to 0.0025 cm^2/s at 25 °C. In addition, at each temperature, the Convex specimens provide highest thermal diffusivity among the three types of specimens due to the largest solid to powder mass ratio, followed by 1Cone-1.0 and Concave, successively.

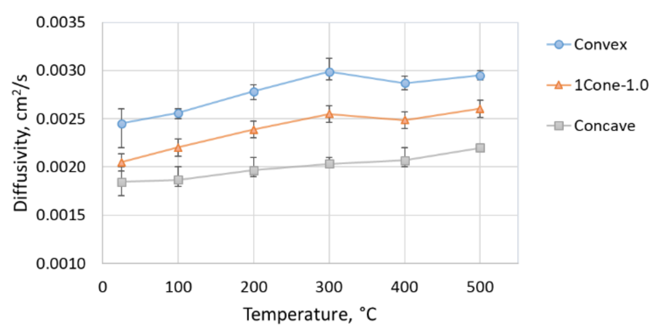

FIGURE 2: COMPARISON OF HOMOGENEOUS TOTAL SAMPLE THERMAL DIFFUSIVITY OF SAMPLES WITH DIFFERENT INTERNAL GEOMETRIES

Furthermore, the time-response thermograms (normalized pyrometer voltage) were obtained from the experiments. Figure 3 (a) shows the thermograms at five tested temperatures of Concave specimens as an example. It can be noted that the plots shift to the left gradually with an increasing temperature; the peak temperature occurs sooner, from 22 s at 100 °C to 16 s at 500 °C, indicating an increase in sample thermal diffusivity. Besides, at a certain temperature, the thermogram of the Convex specimen exhibits a faster heating rate than the other two, and the Concave shows the slowest, corresponding to the thermal diffusivities shown in Figure 2. An example of the comparison between the three cone geometrical specimens at 200 °C is shown in Figure 3 (b).

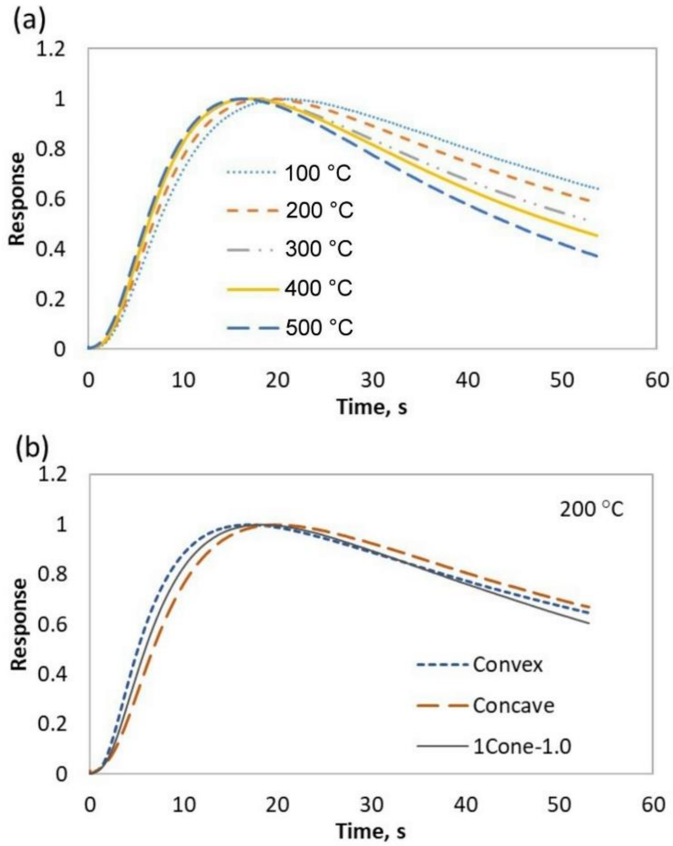

FIGURE 3: EXPERIMENTAL THERMOGRAMS FOR (A) CONCAVE SPECIMENS AT TESTED TEMPERATURES; AND (B) THREE TYPES OF SPECIMENS AT 200 °C

4.2 Simulation results

The FE model was established using measured dimension of the as-built specimens fabricated by L-PBF, and the material properties of the specimens were employed using the information of solid 17-4PH material [29, 30] in Figure 4. Radiation heat loss boundaries assumed an emissivity for 17-4PH of 0.2 [31], and the convection coefficient was estimated as 10 W/(m^2·K) [25]. In addition, the alumina sample holder was included in the modeling and applied the material properties of alumina [32-34].

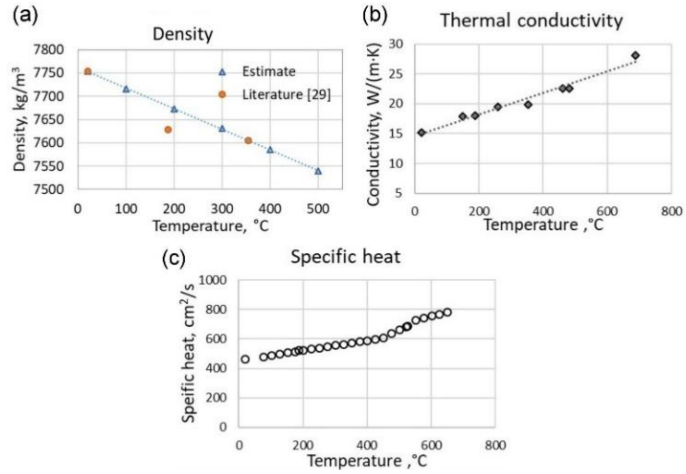

FIGURE 4: SOLID MATERIAL PROPERTIES FOR 17-4PH USED FOR SHELL STRUCTURE IN THE FINITE ELEMENT MODELS [29, 30].

4.2.1 Powder thermal conductivity with different cone geometries

The extracted powder thermal conductivity using the inverse heat transfer method applied to the three new cone designs and is shown in Figure 5. The powder conductivity achieved ranges from 0.65 W/(m·K) to 1.34 W/(m·K), and displays a linear increase with temperature. Additionally, the Convex specimen presents about 0.22 W/(m·K) to 0.31 W/(m·K) higher thermal conductivity than Concave at corresponding temperatures, with the 1Cone-1.0 model located in the middle of the range.

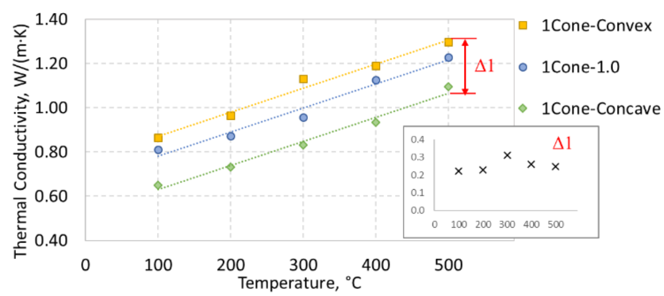

FIGURE 5: POWDER THERMAL CONDUCTIVITY COMPARISON IN 3 NEW CONE GEOMETRIES (INLAYED PLOT USES THE SAME COORNIDATE UNITS WITH THE MAJOR PLOT)

The powder thermal conductivity using the three models in [1] is shown in Figure 6. Similar to the other three models and the two materials in [1], the powder thermal conductivity also exhibits nearly linear to the temperature. Meanwhile, the two models of 2Cone-0.25 (2 cones, 0.25 mm cone height) and 1Cone-0.5 present similar simulation results that are generally lower than 2Cone-0.5 model. The difference (Δ2) between 2Cone-0.5 specimen and the other two is in a range of 0.10 W/(m·K) to 0.19 W/(m·K). It is indicated that the difference with new cone configurations generally shows 35 % wider (Δ1>Δ2).

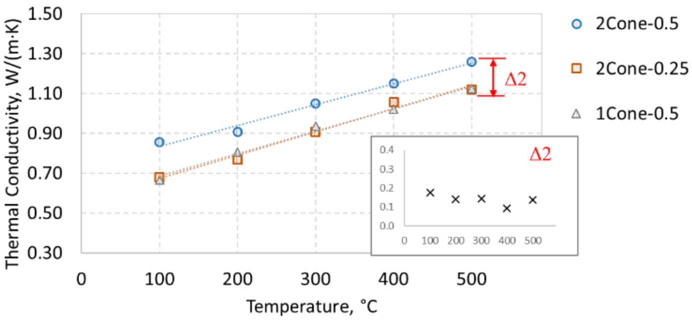

FIGURE 6: POWDER THERMAL CONDUCTIVITY COMPARISON IN 2CONE-0.5, 2CONE-0.25 AND 1CONE-0.5 MODELS (INLAYED PLOT USES THE SAME COORNIDATE UNITS WITH THE MAJOR PLOT)

4.2.2 Analysis of powder conductivity ratio ($\Delta k/k_{ref}$) vs. cone volume ratio ($\Delta V/V_{ref}$) upon the reference model

Stemming from the apparent specimen geometry effect, further investigation on powder thermal conductivity of 17-4PH powder results are analyzed in this section. The cone volume (V) was estimated by taking the difference between the measured mass of the sample, and that of a hypothetical hollow disk of the same external geomery, but 0.5 mm thick skin (and no cone structure). For example, the cone volume of 1Cone-0.5 model was calculated using the cone geometry with a cone height of 0.5 mm. To compare between the different specimens, 1Cone-1.0 specimen was set as the reference (named as "ref"). A measurement criterion was set as a ratio of $\Delta k/k_{ref}$, where k_{ref} is the thermal conductivity of the reference specimen, and Δk equals the objective conductivity value subtracted by that of the reference at the corresponding temperature. Likewise, the volume ratio ($\Delta V/V_{ref}$) is defined based upon the cone volume of the reference. The $\Delta k/k_{ref}$ ratio vs. $\Delta V/V_{ref}$ ratio was plotted in Figure 7. At 100 °C, it is noticed that $\Delta k/k_{ref}$ ratios of 2Cone-0.25 and 1Cone-0.5 are close at about 16 % to 17 %. Concave has a distinguishable (2%) lower $\Delta k/k_{ref}$ ratio despite little difference in $\Delta V/V_{ref}$. Additionally, compared to the reference, 2Cone-0.5 shows higher $\Delta k/k_{ref}$ with about 3 % variation. On the other hand, unlike to the three models with smaller cone volume, the Convex model shows about only 6 % $\Delta k/k_{ref}$ above the x-axis, while the cone volume is about 1.5 times of the reference specimen. Similar quantitative analysis at 100 °C shows the unbalanced $\Delta k/k_{ref}$ ratio at both sides of the y-axis although the $\Delta k/k_{ref}$ ratio for smaller cone models exhibits smaller difference than those at 500 °C. Therefore, such a non-linear correlation between $\Delta k/k_{ref}$ ratio, and reduced difference in this ratio with different cone geometries at higher $\Delta V/V_{ref}$ ratio indicates more reliability of the powder conductivity measurement at a higher cone volume level, such as for the Convex specimens.

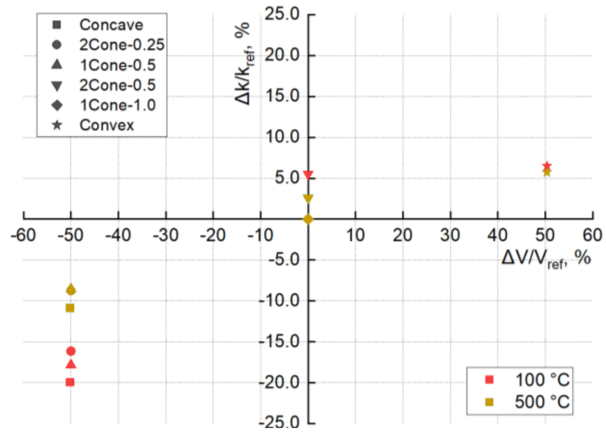

FIGURE 7: $\Delta K/K_{REF}$ VS. CONE VOLUME RATIO AT 100 °C AND 500 °C

4.2.3 Powder thermal conductivity in different materials

Normalized by the solid thermal conductivity (k_s) of the respective powder materials, the powder thermal conductivity ratio (k/k_s) with respect to the fabricated materials in 2Cone-0.5 samples is compared in Figure 8. It can be noticed that the k/k_s ratio of IN625 powder shows a temperature-dependent descent with from 6.9 % to 5.2 %. In contrast, 17-4PH powder exhibits a range of 5.0 % to 5.7 % and a slightly increasing trend with an increasing temperature from 100 °C to 500 °C while the resultant difference between both end temperatures appears insignificant. On the other hand, Ti64 powder keeps an approximately constant k/k_s ratio at all tested temperatures, and the value of the ratio is close to that of 17-4PH powder, which is about 5 %.

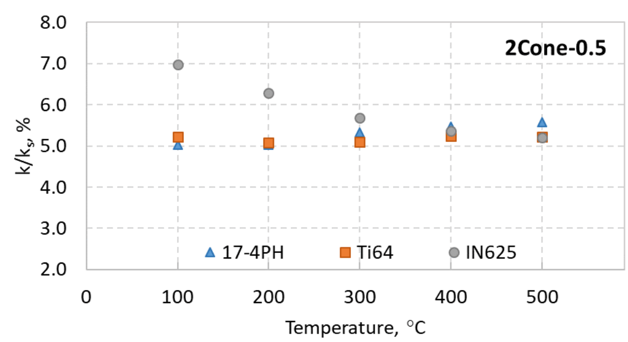

FIGURE 8: COMPARISON OF TEMPERATURE-DEPENDENT K/K_S RATIO IN 2CONE-0.5 MM MODEL WITH THREE MATERIALS.

Similar to 2Cone-0.5 model, IN625 powder still exhibits a descending k/k_s ratio and 17-4PH powder shows a slightly increasing k/k_s in both of 1Cone-0.5 and 2Cone-0.25 models from 100 °C to 500 °C. However, in both models, Ti64 powder shows an approximately 0.5 % decreasing k/k_s ratio. In addition, the k/k_s ratio for the models of 1Cone-0.5 and 2Cone-0.25 in the three powder materials generally reduces 1 % or so due to the internal cone configuration effect. Figure 9 shows the temperature-dependent k/k_s ratio for 2Cone-0.25 models with three powder materials.

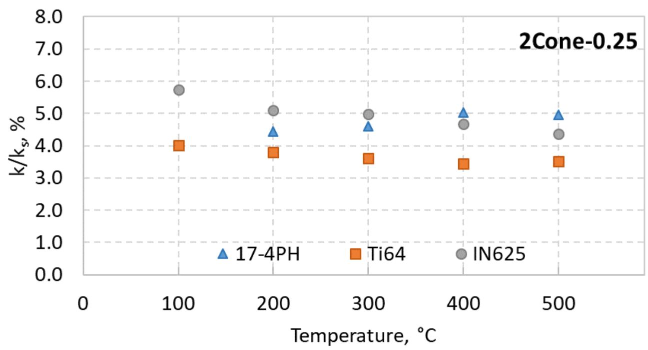

FIGURE 9: COMPARISON OF TEMPERATURE-DEPENDENT K/KS RATIO IN 2CONE-0.25 SPECIMEN WITH THREE MATERIALS

4.2.4 Thermal contact conductance comparison

It has been recognized that the contact conductance is a function of several parameters, such as contacting interface geometry, surface roughness, temperature, interfacial pressure, etc. [35-39]. In the multivariate inverse method, as another two outputs from the simulation, thermal contact conductance between the powder and solid shell on the top and at the bottom are principal parameters interfering with heat transfer in the powder-enclosed specimens. Among the three new specimen geometries, the top and bottom contact conductance are compared in Figure 10. It is noticed that the bottom contact conductance values vary little between the three specimens at each temperature, but overall increase with temperature. The reason for the similar bottom conductance could be that the three specimens have the same bottom geometry. Besides, the bottom contact conductance in all three specimens shows a temperature-dependent increase from 100 °C to 300 °C. Subsequently, there exists a slight retrogression at 400 °C and then a rebound at 500 °C. This trend was also observed for the measured total sample homogeneous thermal diffusivity in Figure 2, indicating this contact conductance may either be a major contributor to the total diffusivity, or may be similarly affected by intrinsic temperature dependence of the material thermal properties.

On the other hand, for the top contact conductance, Convex exhibits apparent higher values than the other two specimens at all tested temperatures; wherein, 1Cone-1.0 shows a higher or similar (at 500 °C) values than Concave. Likewise, at 400 °C, a retrogression or stagnation occurs at 400 °C for all three specimens, followed by an increasing at 500 °C.

Moreover, the contact conductance (top and bottom) were compared between Ti64, IN625 and 17-4PH, and an example of 2Cone-0.25 for the three materials is shown in Figure 11. It can be seen that the bottom contact conductance for all three materials are generally higher than that on the top of the internal powder and solid shell. This is considered to result from a gap that exists between the top shell and the internal powder, interfering the heat transfer through the specimens. Additionally, the retrogression also occurs in 17-4PH 2Cone-0.25 specimen at 400 °C, while such a phenomenon is not found in the other two materials.

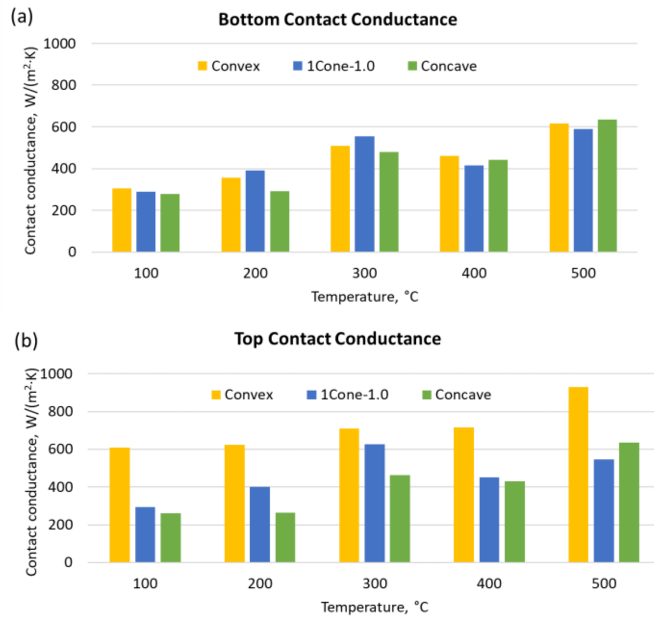

FIGURE 10: SIMULATED CONTACT CONDUCTANCE (A) AT THE BOTTOM, AND (B) ON THE TOP OF THE INTERNAL POWDER AND SOLID SHELL

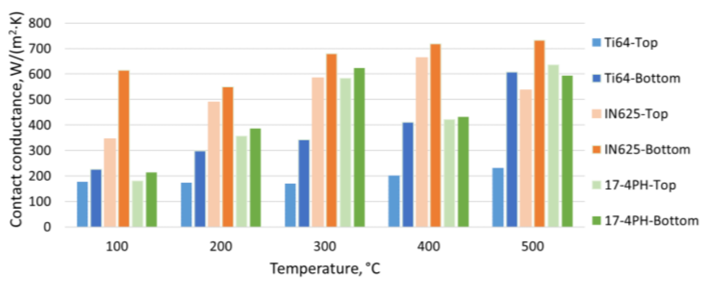

FIGURE 11: CONTACT CONDUCTANCE EVALUATION IN THREE MATERIALS

4.2.5 HEAT TRANSFER IN SPECIMENS

As the transient heat flux is exposed at the bottom of the specimens, the heat flux dissipates through the bottom shell towards the internal powder, and a lower temperature band occurs along the contact surfaces of the three specimens. It is observed that at t = 2.183 s, the internal powder takes heat, spreading upwards slowly due to limited heat transfer at the contact region, with the center region leading higher temperature and dissipation around the center. Additionally, the side shell provides more ability to carry heat to the upper shell, and thus the powder about the edge shows higher temperature for the three specimens. However, apparently, Convex gives a faster thermal flow passing through, followed by 1Cone-1.0 and Concave in an order. At t = 24.863 s, the heat transfer reaches steady state in Convex, and nearly so in Concave and 1Cone-1.0 specimens.

The corresponding heat flux distribution in the middle cut-off areas of the 3 internal powders is shown in Figure 12. At t = 0.011 s, the heat flux starts showing up at the bottom of the internal powders in the three specimens, and not obviously different in values. As the heat is outspreading, heat flux vectors of approximately 6.7 W/m^2 occasionally occurs around the central powder at about 0.1 s in all three specimens. Sequentially, at t = 2.183 s, the energy flows increase in the powder, and the middle portion of the powder shows a higher heat flow rate. Compared to the other two cone featured internal powders, the Concave specimen exhibits a narrower region specifying high heat flux value between 4.0 W/m^2 and 5.0 W/m^2, as the double-arrows are shown in Figure 12.

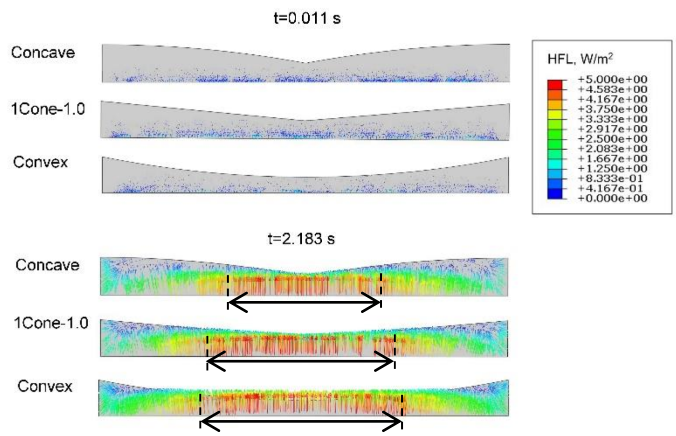

FIGURE 12: HEAT FLUX DISTRIBUTION IN POWDERS IN THREE CONE FEATURED SPECIMENS AT DIFFERENT TIMES

On the other hand, at t = 2.183 s, the heat flux exhibits significantly different on the top of the outer shells with different cone configurations, as shown in Figure 13. In Convex specimen, the heat flux displays a higher value, approximately 2.5 W/m^2 at the boundary that contacts the internal powder, and gradually reduces to none upwards but increases laterally toward outside. The heat flux in the top shells of 1Cone-1.0 and Concave specimens also exhibits the similar transition, but the heat flux at the bottom boundaries is lower than that in Convex. The bottom shells for the three cone featured specimens display insignificant differences. Beyond the range of the heat flux value of interest, the heat flux vectors in the solid shells follow the path along the geometries, and the magnitudes can reach nearly 57 W/m^2 on the side and peripheral of the bottom in the three specimens.

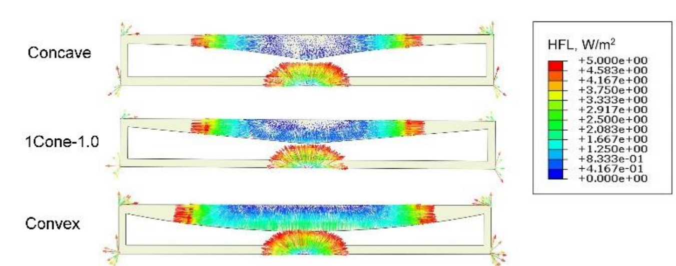

FIGURE 13: HEAT FLUX DISTRIBUTION IN OUTER SHELLS IN THE THREE CONE FEATURED SPECIMENS AT T=2.183 S

In addition, it has been known that the heat flux passing through two contacting objects can be measured as a function of the contact conductance between the two neighboring objects and their temperature gradient. The findings of the heat flux distributed in the shells demonstrate the corresponding tendency of the contact conductance in the three specimens, indicating that the top contact conductance in the Convex specimen exhibits significantly higher than those in 1Cone-1.0 and Concave specimens; although the bottom contact conductance in the three specimens does not vary apparently.

5. CONCLUSIONS

In the present study, hollow specimens were designed with various internal geometries and fabricated with powder enclosed using 17-4PH stainless steel in an L-PBF system. The as-built specimens were tested in a laser-flash equipment to measure the thermal diffusivity up to 500 °C. Then, the combined experimental-numerical simulation was carried out to evaluate the thermal conductivity of the internal powder at 100 °C to 500 °C. An internal geometry effect on the measurement of the metallic powder thermal properties has been analyzed. The contact conditions between the internal powder and the top shell of the specimens exhibited variation between different internal geometrical specimens, which may have resulted in various heat transfer behaviors. The detailed experimental and simulated results are concluded as follows:

- Thermal diffusivity for the 17-4PH specimens with different internal geometries varies from 0.0018 cm^2/s to 0.0025 cm^2/s at 25 °C; wherein, Convex shows the highest values, followed by 1Cone-1.0 and Concave in a descending order at all tested temperatures. As noticed, the thermal diffusivity increases from the room temperature until a plateau at 400 °C, and subsequently increases slightly at 500 °C.
- For each cone configuration specimen, time-response thermograms show an increasing heating rate as temperature rises, with the curves shift to the left, indicative of the rise in sample thermal diffusivity.
- The powder thermal conductivity of 17-4PH is measured ranging from 0.65 W/(m·K) to 1.34 W/(m·K) at 100 °C to 500 °C and displays a linear temperature-dependent tendency for each cone configuration. Specimen geometry has an effect on the powder conductivity evaluation, showing that Convex gives the highest values, and Concave, 1Cone-0.5 and 2Cone-0.25 exhibit similarly lowest.
- As a function of the cone volume, thermal conductivity ratio shows increase with cone volume, although a compromise occurs at the largest cone volume (Convex), and thus appears a non-linear correlation.
- 17-4PH is represented a conductivity ratio of 5.0 % to 5.7 % for 2Cone-0.5 and 4.0 % to 5.0 % for 2Cone-0.25, respectively, which are comparable with Ti64 and IN625 powders at the tested temperatures.
- The bottom contact conductance exhibits similar for the same bottom geometry in different specimens. However, there is variation of the top contact conductance upon

different cone geometries, for example, Convex shows significantly higher top contact conductance. Additionally, the retrogression for both contact conductance in 17-4PH specimens was noticed at 400 °C while this is not the case for Ti64 and IN625.

- Heat flux vectors in the powder of the Convex specimen at t = 2.183 s occurred in a larger region than those in 1Cone-1.0 and Concave specimens. The maximum heat flux value is approximately 5 W/m^2.
- Heat flux in the three cone featured specimens demonstrated the measurement of contact conductance between the internal powder and the outer shell from the developed experimental-numerical approach. Higher top contact conductance in Convex was evaluated than Concave and 1Cone-1.0 specimens, while similar bottom contact conductance was found in the three specimens.

ACKNOWLEDGEMENTS

This research was partially supported by NIST (CA No. 70NANB16H029). The technical support from the computational resource from Cardinal Research Cluster (CRC) at University of Louisville was acknowledged.

REFERENCES

[1] Zhang, Shanshan, Brandon Lane, Justin Whiting, and Kevin Chou, *On thermal properties of metallic powder in laser powder bed fusion additive manufacturing.* Journal of Manufacturing Processes, 2019. **47**: p. 382-392.
[2] *ISO / ASTM52910-18, Additive manufacturing - Design - Requirement, guidelines and recommendations.* ASTM International, West Conshohocken, PA, 2018.
[3] Li, Yali and Dongdong Gu, *Thermal behavior during selective laser melting of commercially pure titanium powder: Numerical simulation and experimental study.* Additive Manufacturing, 2014. **1**: p. 99-109.
[4] Das, Mitun, Vamsi Krishna Balla, Debabrata Basu, Susmita Bose, and Amit Bandyopadhyay, *Laser processing of SiC-particle-reinforced coating on titanium.* Scripta Materialia, 2010. **63**(4): p. 438-441.
[5] Fischer, P, Valerio Romano, Hans-Peter Weber, NP Karapatis, Eric Boillat, and Rémy Glardon, *Sintering of commercially pure titanium powder with a Nd: YAG laser source.* Acta Materialia, 2003. **51**(6): p. 1651-1662.
[6] Dilip, JJS, Shanshan Zhang, Chong Teng, Kai Zeng, Chris Robinson, Deepankar Pal, and Brent Stucker, *Influence of processing parameters on the evolution of melt pool, porosity, and microstructures in Ti-6Al-4V alloy parts fabricated by selective laser melting.* Progress in Additive Manufacturing, 2017: p. 1-11.
[7] Rafi, HK, NV Karthik, Haijun Gong, Thomas L Starr, and Brent E Stucker, *Microstructures and mechanical properties of Ti6Al4V parts fabricated by selective laser melting and electron beam melting.* Journal of materials engineering and performance, 2013. **22**(12): p. 3872-3883.
[8] Zhang, Shanshan, Santosh Rauniyar, Subin Shrestha, Aaron Ward, and Kevin Chou, *An experimental study of tensile property variability in selective laser melting.* Journal of Manufacturing Processes, 2019.
[9] Cheng, Bo and Y Kevin Chou. *Overhang support structure design for electron beam additive manufacturing*. in *ASME 2017 12th International Manufacturing Science and Engineering Conference collocated with the JSME/ASME 2017 6th International Conference on Materials and Processing*. 2017. American Society of Mechanical Engineers Digital Collection.
[10] King, Wayne, Andrew T Anderson, Robert M Ferencz, Neil E Hodge, Chandrika Kamath, and Saad A Khairallah, *Overview of modelling and simulation of metal powder bed fusion process at Lawrence Livermore National Laboratory.* Materials Science and Technology, 2015. **31**(8): p. 957-968.
[11] Whitaker, Stephen, *Local thermal equilibrium: an application to packed bed catalytic reactor design.* Chemical Engineering Science, 1986. **41**(8): p. 2029-2039.
[12] Li, Chi-Hsiung and Bruce A Finlayson, *Heat transfer in packed beds—a reevaluation.* Chem. Eng. Sci, 1977. **32**(9): p. 1055-1066.
[13] Whitaker, S, *Heat and mass transfer in granular porous media.* Adv. Drying, 1980. **1**: p. 23-61.
[14] Klinkenberg, Adrian, *Heat transfer in cross-flow heat exchangers and packed beds.* Industrial & Engineering Chemistry, 1954. **46**(11): p. 2285-2289.
[15] Willhite, GP, Daizo Kunii, and JM Smith, *Heat transfer in beds of fine particles (heat transfer perpendicular to flow).* AIChE Journal, 1962. **8**(3): p. 340-345.
[16] Schotte, William, *Thermal conductivity of packed beds.* AIChE Journal, 1960. **6**(1): p. 63-67.
[17] Masamune, Shinobu and JM Smith, *Thermal conductivity of beds of spherical particles.* Industrial & Engineering Chemistry Fundamentals, 1963. **2**(2): p. 136-143.
[18] Yagi, Sakae and Daizo Kunii, *Studies on effective thermal conductivities in packed beds.* AIChE Journal, 1957. **3**(3): p. 373-381.
[19] Zhou, Jianhua, Aibing Yu, and Yuwen Zhang, *A boundary element method for evaluation of the effective thermal conductivity of packed beds.* Journal of Heat Transfer, 2007. **129**(3): p. 363-371.
[20] Wakao, N and D Vortmeyer, *Pressure dependency of effective thermal conductivity of packed beds.* Chemical Engineering Science, 1971. **26**(10): p. 1753-1765.
[21] Hadley, G R_, *Thermal conductivity of packed metal powders.* International Journal of Heat and Mass Transfer, 1986. **29**(6): p. 909-920.
[22] Vargas, Watson L and Joseph J McCarthy, *Heat conduction in granular materials.* AIChE Journal, 2001. **47**(5): p. 1052-1059.
[23] Wei, Lien Chin, Lili E Ehrlich, Matthew J Powell-Palm, Colt Montgomery, Jack Beuth, and Jonathan A Malen, *Thermal conductivity of metal powders for powder bed additive manufacturing.* Additive Manufacturing, 2018. **21**: p. 201-208.

[24] Bala, Kanan, Pradeep R Pradhan, NS Saxena, and MP Saksena, *Effective thermal conductivity of copper powders.* Journal of Physics D: Applied Physics, 1989. **22**(8): p. 1068.
[25] Cheng, Bo, Brandon Lane, Justin Whiting, and Kevin Chou, *A Combined Experimental-Numerical Method to Evaluate Powder Thermal Properties in Laser Powder Bed Fusion.* Journal of Manufacturing Science and Engineering, 2018. **140**(11): p. 111008.
[26] Zhang, Shanshan, Brandon M Lane, Justin G Whiting, and Kevin Chou. *An Investigation into Metallic Powder Thermal Conductivity in Laser Powder Bed Fusion Additive Manufacturing*. in *Solid Freeform Fabrication Symposium*. 2018.
[27] Clark Iii, LM and RE Taylor, *Radiation loss in the flash method for thermal diffusivity.* Journal of Applied Physics, 1975. **46**(2): p. 714-719.
[28] Ozisik, M Necat, *Inverse heat transfer: fundamentals and applications*. 2000: CRC Press.
[29] Rack, HJ, *Physical and mechanical properties of cast 17-4 PH stainless steel*. 1981, Sandia National Labs., Albuquerque, NM (USA).
[30] *17-4PH stainless steel thermal conductivity. Available from: https://www.upmet.com/sites/default/files/datasheets/17-4-ph.pdf.*
[31] Shurtz, Randy, *Total Hemispherical Emissivity of Metals Applicable to Radiant Heat Testing*. 2018, Sandia National Lab.(SNL-NM), Albuquerque, NM (United States).
[32] Han, Quanquan, Rossitza Setchi, Sam L Evans, and Chunlei Qiu, *Three-dimensional finite element thermal analysis in selective laser melting of Al-Al2O3 powder.*
[33] Vora, Hitesh D and Narendra B Dahotre, *Multiphysics theoretical evaluation of thermal stresses in laser machined structural alumina.* Lasers in Manufacturing and Materials Processing, 2015. **2**(1): p. 1-23.
[34] Kieruj, Piotr, Damian Przestacki, and Tadeusz Chwalczuk, *Determination of emissivity coefficient of heat-resistant super alloys and cemented carbide.* Archives of Mechanical Technology and Materials, 2016. **36**(1): p. 30-34.
[35] Holman, Jack P, *Heat transfer*. 2010: McGraw-hill.
[36] Cengel, Yunus A, *Introduction to thermodynamics and heat transfer*. Vol. 846. 1997: McGraw-Hill New York.
[37] Rosochowska, M, R Balendra, and K Chodnikiewicz, *Measurements of thermal contact conductance.* Journal of Materials Processing Technology, 2003. **135**(2-3): p. 204-210.
[38] Malinowski, Z, JG Lenard, and ME Davies, *A study of the heat-transfer coefficient as a function of temperature and pressure.* Journal of materials processing technology, 1994. **41**(2): p. 125-142.
[39] Zavaliangos, Antonios, Jing Zhang, Martin Krammer, and Joanna R Groza, *Temperature evolution during field activated sintering.* Materials Science and Engineering: A, 2004. **379**(1-2): p. 218-228.